High-speed side-shooter using Leidenfrost phenomena

Hideyuki Sugioka (iD), Satoru Segawa, and Mako Kubota

View Online

Export Citation

CrossMark

High-speed side-shooter using Leidenfrost phenomena

Hideyuki Sugioka,[a] Satoru Segawa, and Mako Kubota

AFFILIATIONS

Department of Mechanical Systems Engineering, Shinshu University, 4-17-1 Wakasato, Nagano 380-8553, Japan

[a]Electronic mail: hsugioka@shinshu-u.ac.jp

ABSTRACT

Liquid delivery systems are important in microfluidic applications. In this paper, we report a high-speed side-shooter using a simple plate-like hot protrusion placed on the lower edge of a hot slope. In particular, we experimentally show that the side-shooter launches a droplet with a high speed (~ 15 cm/s). We propose a simple model to explain the side-shooting phenomenon; i.e., the hot protrusion causes an increase in the surface energy due to the formation of a new folded surface, which results from a new Leidenfrost phenomenon coupled with the protrusion, and therefore, the droplet can be launched at a high speed on the hot slope with a low friction due to the ordinary Leidenfrost phenomenon. A comparison of the theoretical results with the experimental results shows that they are in good agreement with each other. We believe that our side-shooter will play an important role in microfluidics in the future.

I. INTRODUCTION

The development of miniaturized high speed liquid delivery systems is essential for integrated microfluidic systems such as lab-on-a-chip and micrototal analysis systems (μTAS).[1] Therefore, various studies have been devoted to this purpose, ranging from the classical dc electro-osmotic pumps[2] to the challenging liquid delivery systems.[3–5] Nevertheless, the typical flow velocity of a dc-electro-osmotic (DCEO) pump is still in the order of 0.1 mm/s, and even the improved ac-electro-osmotic (ACEO) pump just produces a flow velocity of the order of 1 mm/s.[3] Although electro-wetting actuators have demonstrated average velocities of 3 cm/s by using the electro-wetting phenomenon,[4] they require high voltages (e.g., 40–80 V) with a corresponding matrix driving system, which may increase the cost of the system significantly. Linke *et al.*[5,6] reported the self-propelled motion of a droplet at ~ 5 cm/s on hot surfaces with an asymmetric ratchet-like topology over the Leidenfrost temperature. This has attracted considerable attention, and extensive studies ranging from fundamental studies to application research have been conducted on this topic.

For example, Ok *et al.*[7] reported that submicron Leidenfrost ratchets yield water droplet velocities of up to ~ 40 cm/s. Cousins *et al.* reported a trapping phenomenon using a concentric Leidenfrost ratchet.[8] Furthermore, with regard to the mechanism, Wüger showed the possibility of thermal creep by performing an analytical evaluation of the temperature distribution.[9] By using the Boltzmann equation, Hardt *et al.* showed that the dominant factor is the pressure-driven flow.[10] By using the lattice Boltzmann modeling, Li *et al.* clearly showed that the motion of self-propelled Leidenfrost droplets is due to the asymmetry of the ratchets and the vapor flows beneath the droplets.[11] It should be noted that the Leidenfrost phenomenon is a kind of film boiling phenomena of a droplet on a hot plane substrate. Furthermore, it is characterized by the hovering state of the droplet and the long lifetime of the droplet over the Leidenfrost temperature T_L; e.g., $T_L \sim 150\,^\circ$C for a water droplet of diameter 1 mm on a duralumin plate.[12] These two characteristics result from the existence of a vapor layer between the droplet and the substrate due to the evaporation of the droplet and the balance of the heat conduction from the substrate to the droplet.[12] Obviously, Leidenfrost phenomena have much potential to achieve a high-speed liquid delivery system, which cannot be achieved by other phenomena.

In particular, new devices using Leidenfrost phenomena are promising,[6] and innovative studies are being devoted to this problem even now. For example, from the viewpoint of world-wide energy reduction and microfluidic applications, Hashmi *et al.* demonstrated that a small cart on a liquid can be transported at a high speed (~ 16 cm/s) along the hot ratchet surface by utilizing a Leidenfrost phenomenon.[13] Wells *et al.* demonstrated a sublimation

heat engine that works under ultralow friction conditions, inspired by the self-propelled Leidenfrost phenomenon.[14] Shi et al.[15] demonstrated a self-propelled hovercraft based on a cold Leidenfrost phenomenon and suggested that it could be used as a cargo ship or a petroleum contamination collector. Sugioka and Segawa[16] proposed a controllable Leidenfrost glider on a shallow water layer and demonstrated that the vehicle can move at a velocity of ~ 20 cm/s. Arter et al.[17] reported the conditions under which the droplet velocity can exceed 35 cm/s by using a single device with a continuously adjustable ratchet surface. Furthermore, as pointed out by Quéré, controlling ultramobile Leidenfrost drops is one of the main future directions,[6] and from this viewpoint, Luo et al. explored self-propulsion of a Leidenfrost drop between nonparallel structures.[18] In addition, new experimental facts, which suggest the possibility of new self-propelling devices, have been discovered recently. For example, Minal et al.[19] found that a drop on a hot ratchet has a combined motion of translation and self-rotation. Pham et al.[20] observed that hydrogel drops, initially at rest on a surface, spontaneously jump upon rapid heating and continue to bounce with increasing amplitudes. Bouillant et al.[21] reported that Leidenfrost droplets initially at rest on horizontal substrates self-rotate and self-propel in the direction they are rolling.

However, the fundamental design principle for future devices using Leidenfrost phenomena is still unclear. Furthermore, a high speed side-shooter using a hot protrusion has not been explored so far. Therefore, in this study, we propose a high-speed side-shooter based on hot protrusion and clarify its mechanism, which may provide a design principle for future devices with promising performance. Namely, in this study, we focus on a side-shooter based on hot protrusion and experimentally prove that it can shoot a droplet at a high speed (~ 0.15 m/s). Furthermore, we propose a simple self-consistent model that explains the side-shooting phenomenon, which is caused by the formation of a new folding surface due to a new Leidenfrost phenomenon, along with the hot protrusion, and discuss the mechanism.

II. EXPERIMENTAL METHOD

Figure 1(a) shows the proposed side-shooting system (using a Leidenfrost phenomenon), which consists of an oblique hot brass plate with an inclination angle θ ($= 3°$) at temperature $T_{s,1}$ ($\simeq T_s$), a hot protrusion brass plate (placed on the lower edge of the hot slope at the position $X = 0$) at $T_{s,2}$ ($\simeq T_s$), and a hemisphere droplet of water with a radius r_0 ($= 3.15$ mm). More precisely, the brass plate of thickness 1 mm is placed on the surface of a laboratory hot plate, and the brass plate is heated to T_s by the laboratory hot plate; i.e., the temperature T_s ($= 300°C$) is measured on the surface of the laboratory hot plate. In detail, $T_{s,2}$ ($= 298°C$) was measured on the surface of the root of the protrusion by using a thermocouple thermometer in our experiment. Therefore, the relation $T_s \simeq T_{s,1} \simeq T_{s,2}$ is justified within an accuracy of $2°C$; i.e., there is no large difference among T_s, $T_{s,1}$, and $T_{s,2}$, although Auliano et al.[22] reported that there can be a large difference of about $95°C$ between the temperature measured on the surface and the temperature measured in the heating block. Furthermore, by placing the droplet on the slope at $X = X_0$, we observed that the droplet slid down toward the hot protrusion with a very low friction force ($f_v \sim 0$ N) compared with the

tangential projection of the droplet weight due to the ordinary Leidenfrost phenomenon of the hot slope, and after contacting the protrusion, the droplet was launched to the upper position at $X = X_1$ because of the Leidenfrost phenomenon coupled with the new surface formation that accumulated the surface energy due to the surface tension $\gamma = 58.9$ mN/m at the boiling temperature T_b ($= 100°C$) of water. Here, we used deionized water (milli-Q, 18.2 MΩcm). Furthermore, we determined the experimental dependence of the position $X(t)$ on t from the video data of size 1280×720 and frame rate of 240 fps. Specifically, we analyzed the motions of the droplet numerically by using the video data with an image processing technique; i.e., by performing binarization of the video data with a suitable threshold, we detected the droplet pixels and determined the position $X(t)$ of the center of gravity.

Figure 1(b) shows the detailed structure of the protrusion [gap l_1 ($= 1$ mm), thickness l_2 ($= 1$ mm), and depth l_3 ($= 2.5$ mm)] just before the collision of the droplet with the protrusion at $t = t_0$, while Fig. 1(c) shows the deformation of the droplet during the surface formation process of the new Leidenfrost phenomenon. From the video data of the experiment, we determined the maximum push-in widths w_1 and w_2 at the lower and higher positions, respectively, the average push-in width $w_b = (w_1 + w_2)/2$, the corresponding times t_{w1} and t_{w2}, and the average push-in time $t_b = (t_{w1} + t_{w2})/2$. Furthermore, we define the corresponding push-in time periods as $\Delta t_{w10} = t_{w1} - t_0$, $\Delta t_{w11} = t_1 - t_{w1}$, $\Delta t_{w20} = t_{w2} - t_0$, $\Delta t_{w21} = t_1 - t_{w2}$, $\Delta t_{wb0} = t_{wb} - t_0$, and $\Delta t_{wb1} = t_1 - t_{wb}$. In order to observe the surface formation process in detail, we set a video camera having a wide-angle lens in front of the hot protrusion of the side shooter. Since there was a distortion at the edge area of the image, we corrected the position X as $X(X') = h_s(X')X'$, where $h_s(X') = 1 + (h_{s0} - 1)X'/X'_a$ is a correction factor, $X'_a = 4.25$ cm, $h_{s0} = 5/4.25 \simeq 1.176$, and X' is the position before the correction. Furthermore, we observed that the shape of the droplet in air was spherical with a diameter of ϕ (typically, 5 mm); therefore, we determined the average radius r_0 of the hemisphere from the relation $\frac{4}{3}\pi\left(\frac{\phi}{2}\right)^3 = \frac{2}{3}\pi r_0^3$; i.e., $r_0 = 2^{\frac{1}{3}}\frac{\phi}{2}$. Furthermore, the mass m_p of the droplet was determined as $m_p = \frac{4}{3}\pi\left(\frac{\phi}{2}\right)^3\rho$ (typically, 6.26×10^{-5} kg for $\phi = 5$ mm), where $\rho = 957$ kg/m³ is the density of water at $T_b = 100°C$. We repeated the same experiment N_t times under the same condition and labeled $N = 1$–N_t (typically, 10) to differentiate them. Note that as explained in Ref. 12, the droplet on a Leidenfrost vapor layer is nearly spherical in a rest state, when the drop radius $\phi/2$ is smaller than the capillary number a (2.5 mm for water); i.e., a droplet of $\phi = 5$ mm is considered to be nearly spherical in a rest state. However, there exists a large vertical vibration in the droplet in our experiment, and our video observation tells us that as the first step, it should be dealt with as a hemisphere (on average); please see Figs. 2(a) and 2(d) and the explanation in Sec. III.

III. OBSERVATION OF THE SIDE-SHOOTING PHENOMENON

Figure 2 shows the photographs of the side-shooting motions ($N = 4$ in experiment 1). Here, $T_s = 300°C$, $\theta = 3°$, $\phi = 5$ mm, $r_0 = 3.15$ mm, $X_0 = 5$ cm, $l_1 = l_2 = 1$ mm, and $l_3 = 2.5$ mm. Furthermore, we have used almost the same conditions (except X_0)
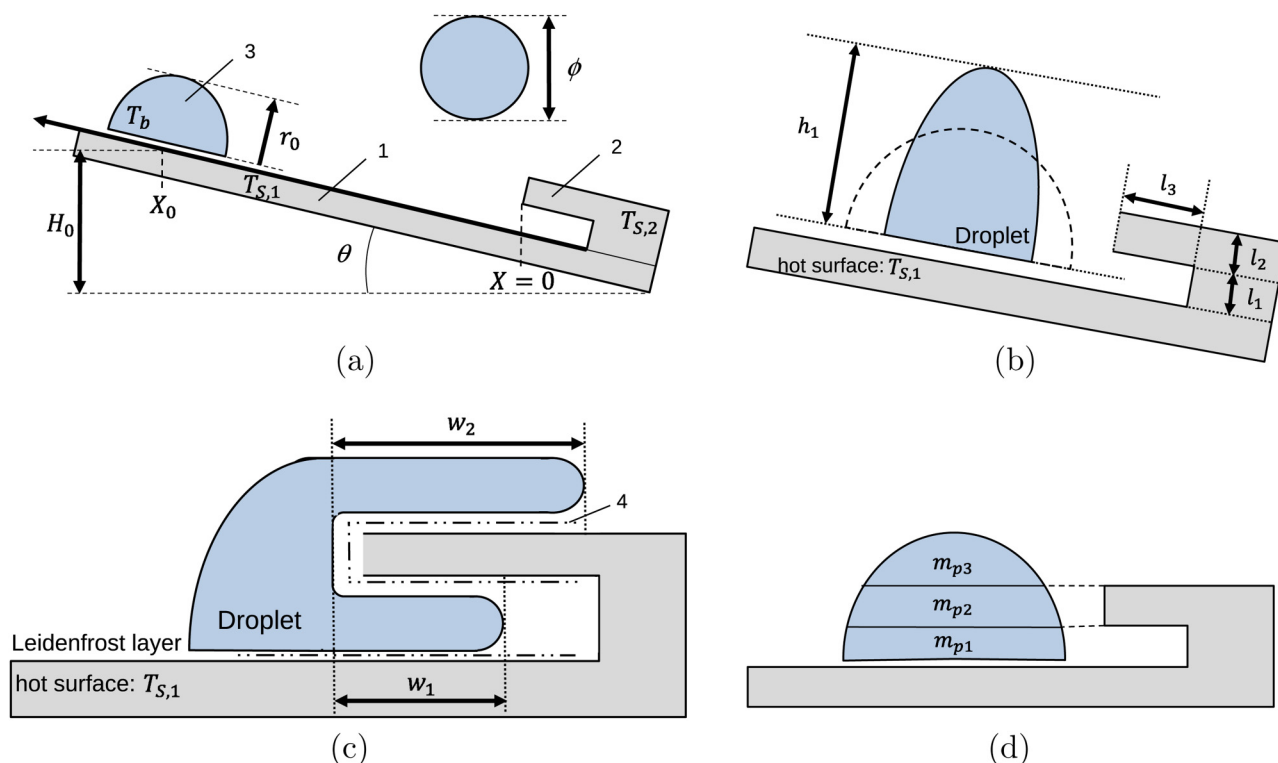
FIG. 1. Schematic view of a side-shooting system using a Leidenfrost phenomenon coupled with a protrusion. (a) Side-shooting system using a new Leidenfrost phenomenon. (b) Structure of the side-shooter using a hot protrusion plate. (c) Accumulation of surface energy due to the formation of a folded vapor layer. (d) Partial masses of the droplet for the calculation of the energy loss ratio. Here, typically, $m_p = 6.26 \times 10^{-5}$ kg, $\rho = 957$ kg/m^3, $g = 9.81$ m/s^2, $\gamma = 58.9$ mN/m at $T_b = 100\,^\circ$C, $T_s \simeq T_{s,1} \simeq T_{s,2} \simeq 300\,^\circ$C (precisely, $T_s = 300\,^\circ$C and $T_{s,2} = 298\,^\circ$C), $\theta = 3^\circ$, $\phi = 5$ mm, $r_0 = 3.15$ mm, $X_0 = 5$ cm, $l_1 = l_2 = 1$ mm, and $l_3 = 2.5$ mm. 1: hot slope, 2: hot protrusion, 3: droplet, 4: folded vapor layer due to a new Leidenfrost phenomenon.

throughout the paper. As shown in Fig. 2(a), the droplet started to slide down from $X = X_0$ at $t = 0$ toward the right edge of the hot slope where friction is almost zero because of the ordinary Leidenfrost phenomenon. Then, it reached the side-shooter at

$X = 0$ at $t = t_0 = 0.483$ s as shown in Fig. 2(b). The droplet was deformed at $t = t_{w1} = t_{w2} = 0.504$ s, as shown in Fig. 2(c). Here, if the temperature of the protrusion $T_{s,2}$ is lower than the Leidenfrost temperature T_L, the vapor layer is not generated, and therefore, a
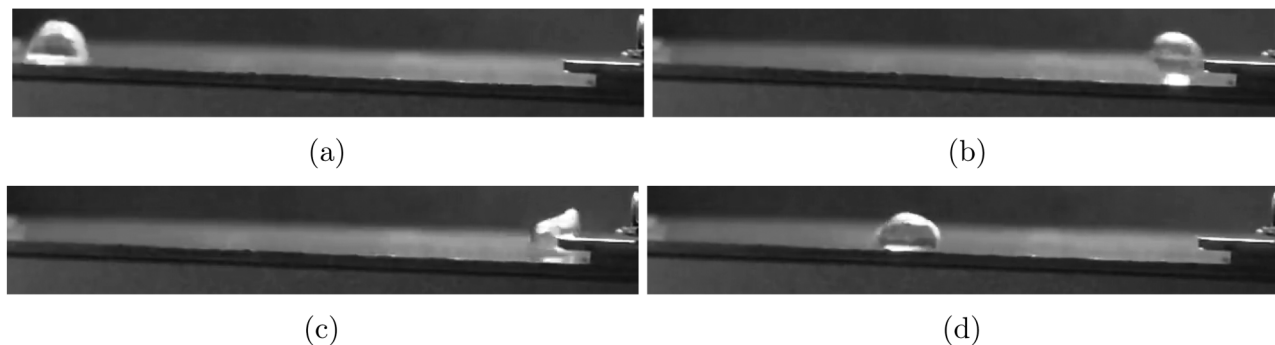

FIG. 2. Photographs of side-shooting motions ($N = 4$ in experiment 1). (a) Initial state at $X = X_0$ ($t = 0$ s). (b) Collision at $X = 0$ ($t = t_0 = 0.483$ s). (c) Deformation ($t = t_{w1} = t_{w2} = 0.504$ s). (d) 1st peak state at $X = X_1$ ($t = 0.883$ s). Here, $T_s = 300\,^\circ$C, $\theta = 3^\circ$, $\phi = 5$ mm, $r_0 = 3.15$ mm, $X_0 = 5$ cm, $l_1 = l_2 = 1$ mm, and $l_3 = 2.5$ mm.

new surface does not appear; as a result, the droplet loses the total kinetic energy, and it cannot be launched. Conversely, at $T_{s,2} > T_L$, the vapor layer is generated and a new surface appears due to the Leidenfrost phenomenon. The well-known Leidenfrost phenomenon does not produce the excess surface energy that can push out the droplet in the lateral direction. Namely, we first observed that the new effect can be found only when a new folded surface is produced by the collaboration between the ordinary Leidenfrost phenomenon and the hot protrusion plate. In other words, the observed phenomenon is a new phenomenon or at least a new type of Leidenfrost phenomena.

IV. SIMPLE MODEL FOR THE SIDE-SHOOTING PHENOMENON

A. Launching performance

To help the readers understand this concept clearly, we explain the theoretical model of the side-shooter before the experimental results. That is, we propose a simple model that explains the side-shooting phenomenon due to a new Leidenfrost phenomenon coupled with the new surface formation process. Since we can neglect the friction force between the droplet and the hot slope caused by the vapor layer due to the ordinary Leidenfrost phenomenon, the velocity of the droplet at $t = t_0$ is

$$V_0 \simeq \sqrt{2gH_0}, \qquad (1)$$

where $g = 9.81 \text{ m/s}^2$ and $H_0 \, (= X_0 \sin \theta)$ is the height of the initial position. Similarly, the velocity of the droplet at $t = t_1$ is $V_1 \simeq \sqrt{2gH_1}$, where $H_1 \, (= X_1 \sin \theta)$ is the height of the first peak position at $X = X_1$. Here, $r_{loss} = E_1/E_o = (H_0 - H_1)/H_0$ represents the energy loss ratio and H_1 is predicted as

$$H_1 \simeq (1 - r_{loss})H_0. \qquad (2)$$

In general, we can write that $H_n \simeq [1 - r_{loss}(H_{n-1})]H_{n-1}$ with $H_n = X_n \sin \theta$, where X_n is the $n (= N_p)$th peak position. Thus, if $r_{loss}(H_{n-1}) \simeq \text{const.}$, we can write $H_n \simeq (1 - r_{loss})^n H_0$. In this case, the corresponding maximum velocity is written as $V_n \simeq \sqrt{2g(1 - r_{loss})^n H_0}$. Note that r_{loss} is constant at $l_3 \gg w_1$ because r_{loss} is mainly determined by the mass ratio, which was stopped by the small vertical wall of the protrusion, as will be explained later. Furthermore, since $X_n = \frac{H_n}{\sin \theta} \simeq \frac{(1 - r_{loss})^n}{\sin \theta} H_0$, the observable travel length becomes small, as θ increases. In other words, if θ becomes too large, we cannot observe the side-shooting phenomenon appropriately. Therefore, in this experiment, we select $\theta = 3°$ as an appropriate condition.

B. Energy loss ratio (Models A and B)

We consider the masses (m_{p1}, m_{p2}, and m_{p3}) of the lower, middle, and upper parts, respectively, of the hemisphere with radius r_0, which have thicknesses of l_1, l_2, and $r_0 - l_1 - l_2$, as shown in Fig. 1(d). By assuming that the kinetic energy of the middle part is lost due to the impinging of the protrusion with thickness l_2 and that the kinetic energy of m_{p1} is converted into the surface energy of the new surface under the protrusion plate of area

$S_w(w, r_0, l_1)$, we obtain

$$r_{loss}^{modelA} \simeq m_{p2}/m_p, \qquad (3)$$

$$\gamma S_w(w, r_0, l_1) \simeq m_{p1}gH_0, \qquad (4)$$

where $S_w(w, r_0, l_1) = f_a(w, \sqrt{r_0^2 - l_1^2})$, w represents the push-in width, and the area function $f_a(w, r)$ $(r = \sqrt{r_0^2 - l_1^2})$ is given by $f_a(w, r) = r^2 \cos^{-1}(1 - \frac{w}{r}) - (r - w)\sqrt{w(2r - w)}$. We call this model as Model A, and it is useful under the condition $w \ll l_3$, whereas under the condition $w \sim l_3$, we need to consider the energy loss of m_{p1} as Model B. Namely, we obtain

$$r_{loss}^{modelB} \simeq \frac{m_{p2} + r_B m_{p1}}{m_p}, \qquad (5)$$

where r_B $(0 \le r_b \le 1)$ is the loss ratio of the kinetic energy of m_{p1}. Here, $m_{p1} = \rho[f_v(r_0, r_0) - f_v(r_0, r_0 - l_1)]$, $m_{p2} = \rho[f_v(r_0, r_0 - l_1) - f_v(r_0, r_0 - l_1 - l_2)]$, and the volume function $f_v(r, h)$ is given by $f_v(r, h) = \frac{\pi}{6}h[3h(2r - h) + h^2]$. Furthermore, we determined $r_B(X_n)$ as $r_B(X_n) \simeq 0.8(X_n/X_{0c})^4$ to explain our experimental results [which will be explained in Fig. 6(b)], where $X_{0c} = 5$ cm; however, since $r_B \le 1$, we set $r_B(X_n) \simeq 0.8(X_n/X_{0c})^4$ at $X_n < 5.29$ cm and $r_B = 1$ at $X_n \ge 5.29$ cm, in Eq. (5). Note that if $w \sim l_3$, r_{loss} is not constant in the sense that $r_B(X_n)$ changes for every impinging event. Furthermore, at the moment of impact, the liquid can transfer some momentum in the lateral directions. However, the kinetic energy in the lateral directions is preserved and converted into the surface energy until the motion of the droplet is stopped. Therefore, the transfer of momentum in the lateral directions needs not be considered in the current problem.

C. Fluctuation model to account for vertical vibration (Model C)

We consider the effect of fluctuation of h_1 [in Fig. 1(b)] due to a vertical vibration of the droplet. Since impinging volume decreases as h_1/r_0 increases, the prediction of r_{loss} is simply corrected as follows:

$$r_{loss}^{modelC}(h_1, r_0) \simeq \frac{r_0}{h_1}\frac{m_{p2} + r_B m_{p1}}{m_p}. \qquad (6)$$

Note that since we observed a relatively large variation of X_1 in the experiment, we need to consider this model (Model C) to recognize the cause, and Eq. (6) successfully explains the fluctuation, as will be presented in Figs. 5(a) and 5(b). Here, since the height of the droplet extends $\frac{h_1}{r_0}$ times in the vertical direction, the length of the middle part of m_{p2} also extends $\frac{h_1}{r_0}$ times; i.e., the deformed length of the middle part of m_{p2} is written as $l_2' = \frac{h_1}{r_0}l_2$. Similarly, the deformed length of the lower part of m_{p1} is written as $l_1' = \frac{h_1}{r_0}l_1$. Since the ratio of the impinging mass m_{p2}' to the mass m_{p2} of the deformed part is in the ratio of l_2 to l_2', we can write $\frac{m_{p2}'}{m_{p2}} = \frac{l_2}{l_2\frac{h_1}{r_0}} = \frac{r_0}{h_1}$. Similarly, we can write $\frac{m_{p1}'}{m_{p1}} = \frac{l_1}{l_1\frac{h_1}{r_0}} = \frac{r_0}{h_1}$. Thus, for the deformed particle, we can write $r_{loss}^{modelC}(h_1, r_0) \simeq \frac{m_{p2}' + r_B m_{p1}'}{m_p} \simeq \frac{r_0}{h_1}\frac{m_{p2} + r_B m_{p1}}{m_p}$.

D. Time model (Model D)

We consider the Lagrange equation of motion during the surface formation process at $t_0 \leq t' \leq t_1$; i.e.,

$$\frac{d}{dt'}\left(\frac{\partial L}{\partial \dot{X}'}\right) - \frac{\partial L}{\partial X'} = 0, \tag{7}$$

where $L (= T - U)$ is the Lagrange function, $T (= \frac{1}{2} m_{p1} \dot{X}'^2)$ is the kinetic energy of m_{p1}, $U (= 2rAr_0\gamma X')$ is the potential energy due to the new surface formation, $\dot{X}' = \frac{dX'}{dt'}$, and the direction of the X' axis is opposite to that of the X axis. Note that since Eq. (4) is slightly inconvenient, we approximate $S_w(w, r_0, l_1) \sim 2Ar_0 w$. Thus, we obtain

$$w^{ModelD} \sim \frac{m_{p1} g H_0}{2Ar_0\gamma}, \tag{8}$$

where $A (= 0.83)$ is the adjustment parameter, which is determined as $A \simeq 0.83$ from the experimental results [in Fig. 6(a)]. From Eq. (7), we obtain

$$m_{p1}\ddot{X}' = -2Ar_0\gamma. \tag{9}$$

Thus, by solving Eq. (9) under the initial condition that $\dot{X}' = V_0 = \sqrt{2gH_0}$ and $X' = 0$ at $t' = 0$, we obtain

$$\dot{X}' = \sqrt{2gH_0} - \frac{2Ar_0\gamma}{m_{p1}} t'. \tag{10}$$

Hence, by considering $\dot{X}' = 0$, we obtain a theoretical push-in time as

$$\Delta t_w^{modelD} = \frac{m_{p1}}{2Ar_0\gamma}\sqrt{2gH_0}. \tag{11}$$

V. EXPERIMENTAL RESULTS

A. Launching effect

Figure 3 shows the launching effect of the side-shooter. In Fig. 3, the symbols and lines show the experimental and theoretical results, respectively. As shown in Figs. 3(a)–3(c), the droplet was experimentally launched to the level of $X_0 \simeq 1.5$–3 cm by the side-shooter, and our prediction using Model C with an average value of $\bar{h}_1/r_0 = 1.29$ explains the observed launching height to some extent, although significant fluctuation exists, as will be discussed later in detail. Figure 3(d) shows the dependence of the velocity $V = \frac{dX}{dt}$ on t, while Fig. 3(e) shows the velocity V_p corresponding to X_p (or H_p). Here, $V_p = \sqrt{2gX_p \sin\theta}$ ($p = 1, 2, 3$) shows the launching velocity calculated from X_p. In Fig. 3(e), the theoretical curve of Model C' is obtained from $V_p(N_p) = \sqrt{2g(1 - r_{loss})^{N_p} X_0 \sin\theta}$ under the assumption that $r_{loss} = r_{loss}^{model C} = 0.603$ with $r_B = r_B(X_0) = 0.898$ in Eq. (6), whereas the theoretical dots ($\times$) of Model C are calculated from $V_p(N_p) = \sqrt{2g(1 - r_{loss}^{model C}) X_{N_p - 1} \sin\theta}$ under the assumption that $r_{loss}^{model C} = r_{loss}^{model C}(X_{N_p - 1})$; e.g., $r_{loss}^{model C} = 0.603, 0.295,$ and 0.285 ($r_B = 0.898, 0.317,$ and 0.007) for $N_p = 1, 2,$ and 3, respectively.

Although the droplet volume decreases gradually with respect to time, the effect seems to be negligible for small N_p values, since the theoretical plot using Model C agrees with the experimental V_p in Fig. 3(e). From Figs. 3(d) and 3(e), we find that the maximum launching velocity is approximately 15 cm/s, and it is comparable to that of the liquid delivery system of Linke et al.,[5] which is much higher than that of other systems. Thus, the performance of our side-shooter is outstanding in spite of the simple structure; e.g., it does not require a sawtooth-like structure on the slope and just needs a hot protrusion. Figure 3(f) shows the experimental trajectory $(x_p(t), y_p(t))$ of the droplet, which was obtained by using the image processing technique; the (red) dots in Fig. 3(f) represent a real droplet trajectory and not a conceptual trajectory. As shown in Fig. 3(f), we can control the trajectory of the droplet freely in a two-dimensional (2D) plane by using the reflection effect of the side-shooters [which is represented by the three rectangular plates in Fig. 3(f)]. In other words, by using multiple side-shooters, we can change the direction of the droplet freely in a 2D plane and design the trajectories at will. Thus, our side-shooter is useful for various microfluidic and biomedical applications. Since we can write that $V_x'^{out} = V_y'^{in}$ [from the momentum conservation in the parallel direction (x' direction) to the protrusion plate of the side shooter] and $V_y'^{out} = \sqrt{2gH_{out}} = \sqrt{2g(1 - r_{loss})H_{in}} = \sqrt{(1 - r_{loss})}V_y'^{in}$ [from Eqs. (1) and (2)], the incident and emergence angles are given by $\theta_{in} = \tan^{-1}\frac{V_y'^{in}}{V_x'^{in}}$ and $\theta_{out} = \tan^{-1}\frac{V_y'^{out}}{V_x'^{out}} = \tan^{-1}\frac{V_y'^{in}}{V_x'^{in}}\sqrt{(1 - r_{loss})}$, respectively, where $(V_x'^{in}, V_y'^{in})$ and $(V_x'^{out}, V_y'^{out})$ are the incident and emergence velocities, respectively. In other words, the reflection effect of the side-shooter is a phenomenon caused by the hot protrusion (which reflects the droplet due to the launching effect of the side-shooter).

B. Surface formation process due to the Leidenfrost phenomenon

Figure 4 shows photographs of the surface formation process due to the new Leidenfrost phenomenon at $t = t_0, t_{w1}, t_{w2},$ and t_1 for $N = 1$ and 2. In Figs. 4(a) and 4(e), $h_1 = 4.23$ and 3.53 mm, respectively; i.e., h_1 was significantly different in each experiment. This is because there exists a vertical vibration in the droplet, which was already explained in detail by using numerical simulations in Ref. 23, and this is the reason for the fluctuation of X_p. Interestingly, the event of higher h_1 (4.23 mm) at $N = 1$ results in a larger w_1 value ($w_1 > w_2$), whereas the event of lower h_1 (3.53 mm) at $N = 2$ results in a larger w_2 value ($w_2 > w_1$), as shown in Figs. 4(c) and 4(g), respectively. This is probably because the droplet of lower h_1 extends in the upper direction in the subsequent period, whereas the droplet of higher h_1 shrinks in the lower direction in the subsequent period. Furthermore, as shown in Figs. 4(b) and 4(f), the kinetic energy of m_{p2} (and a part of m_{p1}) is lost due to the collision with the hot protrusion plate of thickness $l_2 = 1$ mm, as discussed in Sec. IV B. Although the entire energy is usually lost due to the collision in ordinary fluid dynamic systems (as pointed out before), the remaining energy is preserved as the surface energy in the side-shooter because of the formation of a new surface due to the folded Leidenfrost vapor layer resulting from the hot
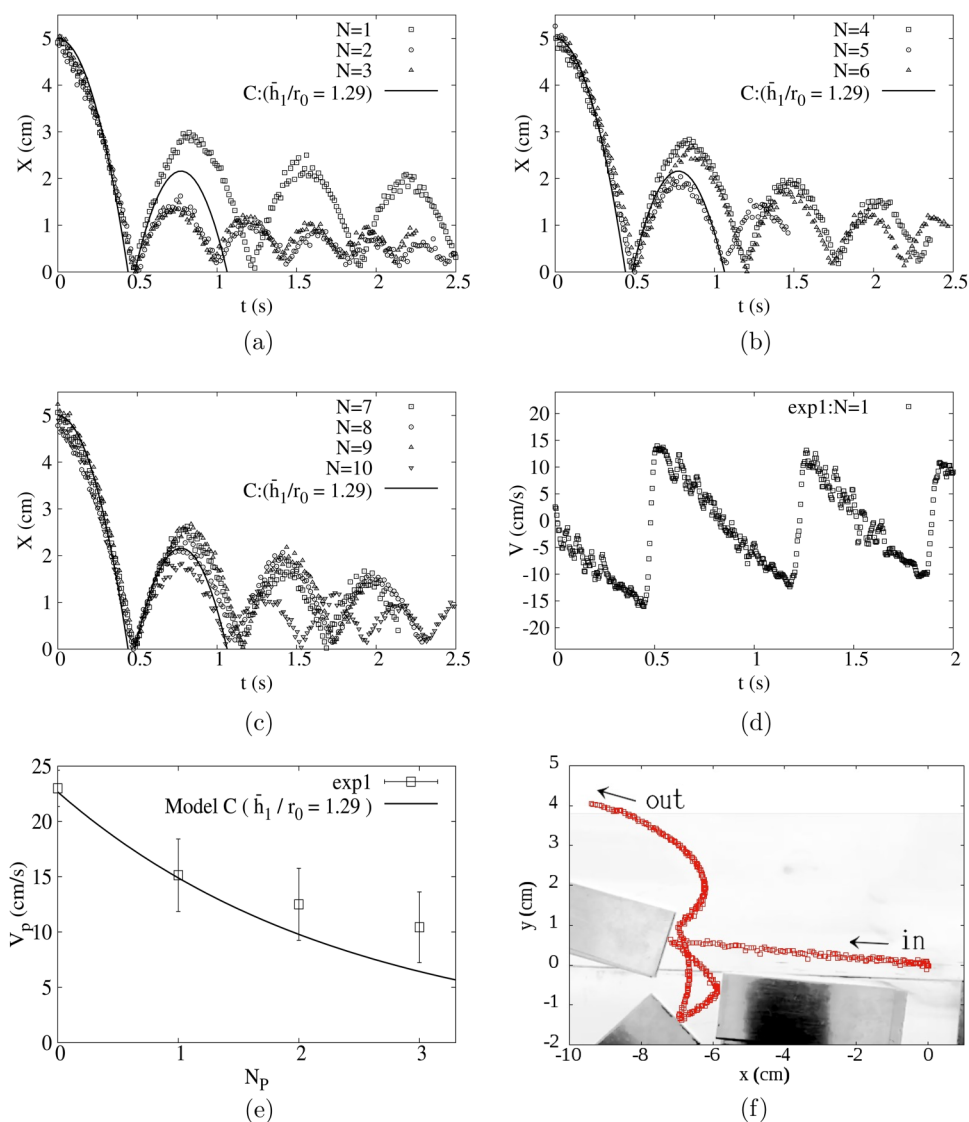
FIG. 3. Launching effect of the side-shooter. (a) X vs t ($N = 1$–3). (b) X vs t ($N = 4$–6). (c) X vs t ($N = 7$–10). (d) V vs t ($N = 1$). (e) V vs N_p. (f) 2D shooting phenomenon due to the reflection phenomenon of the side-shooter. Here, $T_s = 300\,°C$, $\theta = 3°$, $\phi = 5\,mm$, $r_0 = 3.15\,mm$, $X_0 = 5\,cm$, $l_1 = l_2 = 1\,mm$, and $l_3 = 2.5\,mm$.

protrusion plate, and the accumulated surface energy is used for launching the droplet, as shown in Figs. 4(d) and 4(h).

C. Fluctuations due to h₁

Figure 5 shows the fluctuations due to h_1 for two data sets (i.e., Experiments 1 and 2; $N_t = 10$ for each experiment), which were obtained by the same experiment under the same condition on different dates. As shown experimentally in Figs. 5(a) and 5(c), as h_1/r_0 increases, the dependence of H_1 increases, while the energy loss ratio $E_{loss}/E_{in} = (H_0 - H_1)/H_0$ decreases; these experimental results are theoretically explained fairly well by Model C, although there are exceptions. For example, the data set of $h_1/r_0 = 1.42$ and $H_1 = 0.780\,mm$ in Fig. 5(a) for $N = 3$ (in Experiment 1) is an exception. However, we consider that such exceptionally low

values of H_1 occur when $w_2 \gg w_1$ ($w_1 = 3.69\,mm$, $w_2 = 4.62\,mm$ for $N = 3$); i.e., probably because of the fluctuation of the internal flow condition due to the vertical vibration, w_2 becomes much larger than w_1, and in that case, the remaining kinetic energy is not effectively converted into surface energy. Furthermore, Figs. 5(c) and 5(d) show the dependences of w and Δt_w on h_1. Unfortunately, we could not find a clear trend in them. However, in Fig. 5(c), it can be seen that w_1 is limited by $l_3 = 2.5\,mm$, as is considered in Model B, whereas the order of Δt_w is 20 ms as predicted by Model D.

D. Dependences on X₀

Figure 6 shows the dependences on X_0. In Fig. 6, the symbols show the experimental results, whereas the lines show the
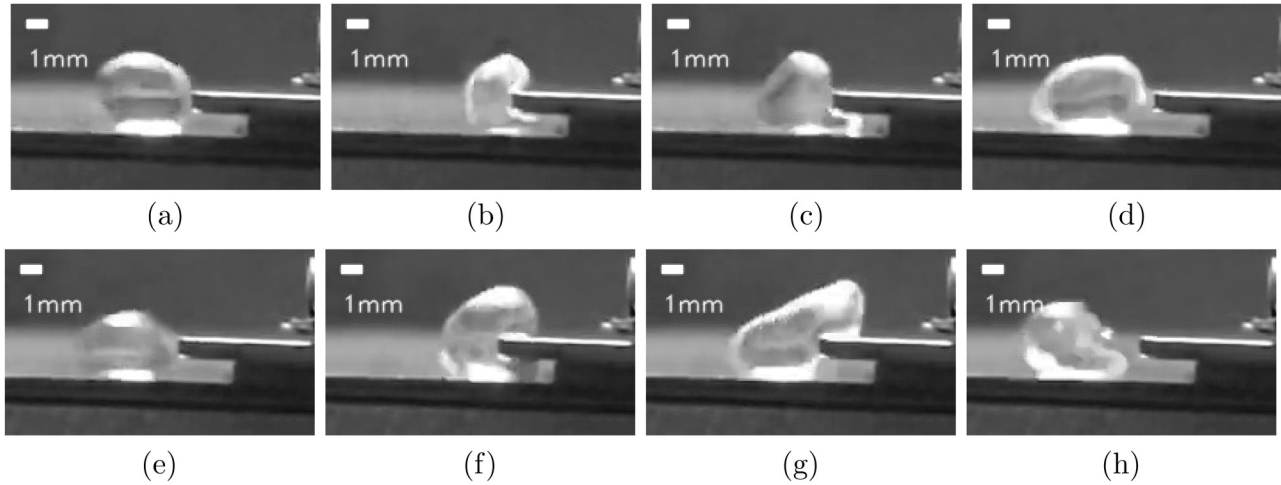
FIG. 4. Surface formation process due to a new Leidenfrost phenomenon. (a) $t = t_0$ ($N = 1$). (b) $t = t_{w2}$ ($N = 1$). (c) $t = t_{w1}$ ($N = 1$). (d) $t = t_1$ ($N = 1$). (e) $t = t_0$ ($N = 2$). (f) $t = t_{w1}$ ($N = 2$). (g) $t = t_{w2}$ ($N = 2$). (h) $t = t_1$ ($N = 2$). Here, $m_p = 6.26 \times 10^{-5}$ kg, $\gamma = 58.9$ mN/m at $T_b = 100\,°C$, $T_s = 300\,°C$, $\theta = 3°$, $\phi = 5$ mm, $r_0 = 3.15$ mm, $X_0 = 5$ cm, $l_1 = l_2 = 1$ mm, and $l_3 = 2.5$ mm; for $N = 1$ ($N = 2$), $\Delta t_{w1} = 0.0029$ s (0.0250 s) and $\Delta t_{w2} = 0.0166$ s (0.0375 s).

theoretical results. As shown in Figs. 6(a)–6(c), the experimental results of the dependences of w, E_{loss}, and H_1 on X_0 agree with the theoretical results fairly well. Specifically, in the experiment, w increases with increase in X_0, and this trend (especially for w_1) is in good agreement with the theoretical prediction by Model A, which

is intrinsically the model for w_1, although w_1 at $X_0 = 5$ cm is experimentally limited by $l_3 = 2.5$ mm. Furthermore, the energy loss ratio E_{loss}/E_{in} [$= (H_0 - H_1)/H_0$] increases with increase in X_0, and this trend is successfully explained by Model B. In addition, the dependence of H_1 on X_0 has a peak at $X_0 = 4$ cm, and this
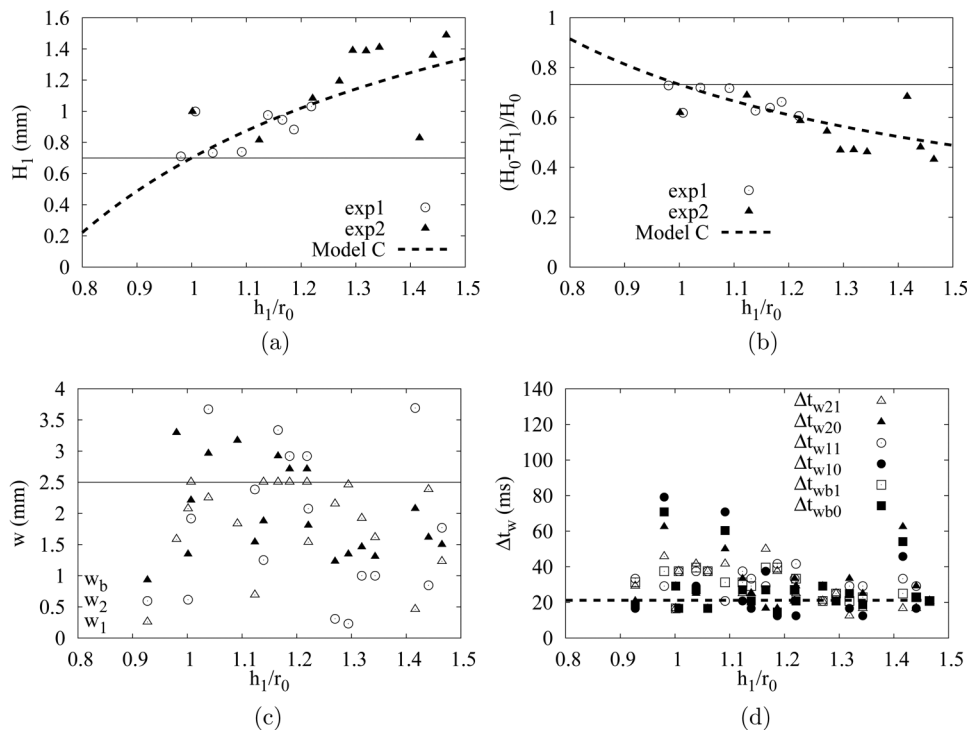

FIG. 5. Fluctuations due to h_1. (a) H_1 vs h_1. (b) E_{loss} vs h_1. (c) w vs h_1. (d) Δt_w vs h_1. Here, $m_p = 6.26 \times 10^{-5}$ kg, $\gamma = 58.9$ mN/m at $T_b = 100\,°C$, $T_s = 300\,°C$, $\theta = 3°$, $\phi = 5$ mm, $r_0 = 3.15$ mm, $X_0 = 5$ cm, $l_1 = l_2 = 1$ mm, and $l_3 = 2.5$ mm. In (a) and (b), the solid lines show the average values using Model C. In (c), the solid line shows the limitation of w_1 due to $l_3 = 2.5$ mm. In (d), the broken line shows the theoretical result using Model D.
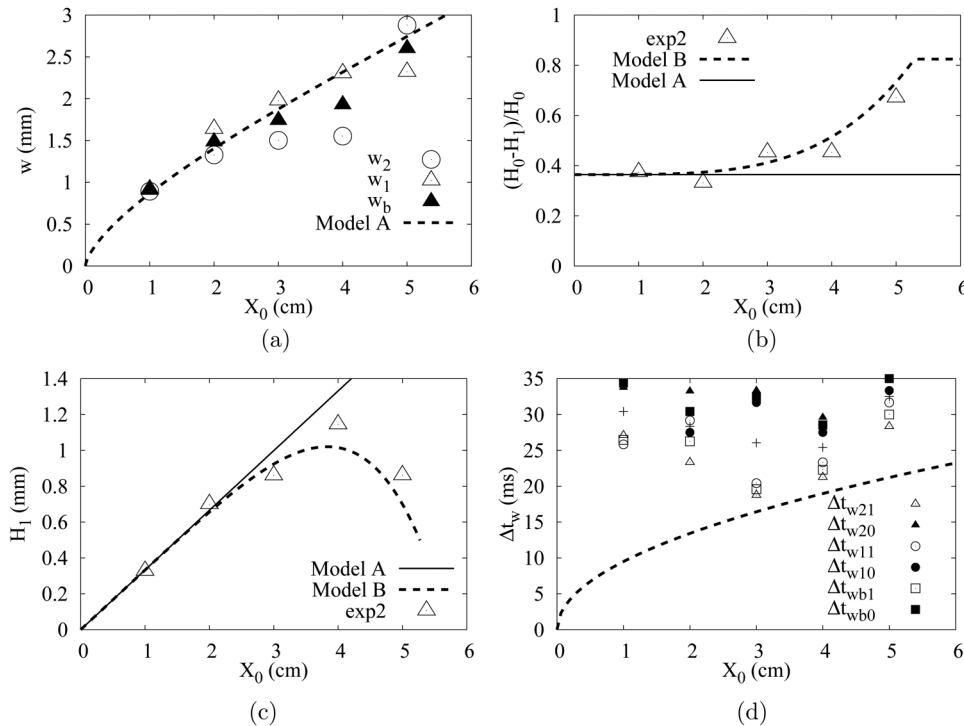
FIG. 6. Dependences on X_0. (a) w vs X_0 ($l_3 = 1$ mm). (b) E_{loss} vs X_0 ($\phi = 5$ mm). (c) H_1 vs X_0 ($\phi = 5$ mm). (d) Δt_w vs X_0 ($\phi = 5$ mm). Here, $m_p = 6.26 \times 10^{-5}$ kg, $\gamma = 58.9$ mN/m at $T_b = 100\,^\circ$C, $T_s = 300\,^\circ$C, $\theta = 3^\circ$, $\phi = 5$ mm, $r_0 = 3.15$ mm, $l_1 = l_2 = 1$ mm, and $l_3 = 2.5$ mm; the symbols show the experimental results, whereas the lines show the theoretical results.

trend is also successfully explained by Model B. Thus, we consider that our simple model is very useful, and the physics of the side-shooting phenomenon is successfully described by our model. However, while the experimental results of the push-in time (Δt_w) is approximately 20–30 ms, our time model (Model D) just predicts the order at $X_0 \geq 3$ cm. This is probably because the energy of the vertical vibration affects Δt_w, and this results in hiding the mean trend of the time model.

VI. DISCUSSION

Although Linke et al.[5] and Ok et al.[7] have already shown high-speed liquid delivery systems of $V \sim 5$ and ~ 40 cm/s, respectively, by using an asymmetrical sawtooth-like structure at $T_{s,1} > T_L$, we were the first to show that a side-shooter having a plate-like hot protrusion can shoot a water droplet with a velocity of ~ 15 cm/s; we have also clarified the side-shooting mechanism. Our side-shooter can shoot the droplet with high velocity by using the accumulated surface energy of the liquid due to the formation of a new folded Leidenfrost vapor layer, which results from a new Leidenfrost phenomenon coupled with the protrusion at $T_{s,1} > T_L$. This mechanism is very different from that of the device of Linke et al., since the liquid droplet (in the device of Linke et al.) is considered to be driven by the pressure-driven flow (due to ∇P)[10] or the thermal creep (due to ∇T).[9]

Moreover, the structure of our side-shooter is very simple; e.g., unlike the device of Linke et al.,[5] our side-shooter does not require sawtooth-like structures on the substrate. Furthermore, unlike the liquid delivery system using an electrowetting phenomenon,[4] our

side-shooter does not require a high-voltage matrix driver and matrix electrodes to apply a strong electric field. In addition, since our side-shooter has a reflection effect [as demonstrated in Fig. 3(f)], there is a possibility that we can realize promising biomedical systems by controlling the trajectories of the droplet at will in a 2D plane in the future. Furthermore, similar to the device of Linke et al.,[5] there is a possibility of developing a system that requires no power supply and operates at a high temperature. Furthermore, similar to the heat engine[14] that uses the principle of the device of Linke et al., a new heat engine that uses our side-shooting mechanism can be realized in the future.

Although a large fluctuation was observed in the launching performance [presented in Figs. 3(a)–3(c)], we can probably suppress the fluctuation in the future, since we have already recognized that the vertical vibration of the droplet is the main cause of the fluctuation [as presented in Figs. 3(a) and 3(b)]. Specifically, the vibration perpendicular to the brass plate results from the nonzero value of the Weber number of the droplet ($We = \frac{\rho \phi U_v^2}{\gamma}$) at X_0, where U_v is the velocity perpendicular to the brass plate at X_0.[23] Therefore, if we place the liquid at X_0 with $U_v = 0$, we can suppress the fluctuation, since $We \sim 0$. Although we tried minimizing the We number in our experiment, it was impossible to place the droplet on the brass plate without generating the vertical vibration, because we cannot remove the needle of the syringe from the droplet at a stable state. If we assume that we need the space $\Delta h (\sim 0.1$ mm) between the upper surface of the droplet and the tip of the needle, we can approximate that $U_v \sim \sqrt{2g\Delta h} \sim 0.04$ m/s and $We \sim 0.2$. Furthermore, if we can use a much smaller droplet in microfluidic
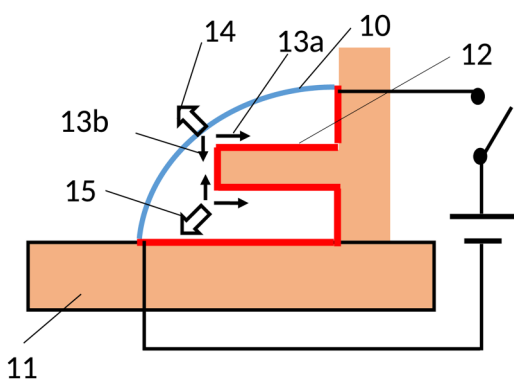
FIG. 7. Schematic view of an active side-shooter using a Leidenfrost phenomenon coupled with a protrusion having a heater. 10: water droplet, 11: substrate (hydrophobic), 12: thin-film heater (hydrophilic), 13a,13b: surface tension at the corner, 14: the net force that works on the droplet at the upper corner, 15: the net force that works on the droplet at the lower corner.

systems, we can also suppress the fluctuation, because We becomes small as ϕ becomes small.

In this paper, we have demonstrated a passive side-shooting system that relaunches a droplet falling onto a protrusion. However, our experimental result clearly shows that we can realize an active side-shooting system that launches a stationary droplet. For example, Fig. 7 shows an active side-shooter that uses a Leidenfrost phenomenon coupled with a protrusion having a heater. As shown in Fig. 7, the thin-film heater has a hydrophilic surface, whereas the substrate has a hydrophobic surface. Thus, we can set the water droplet on the thin-film heater and keep the droplet in a state of rest. Then, we suddenly heat up the droplet with a heat flux of approximately $1\,\mathrm{GW/m^2}$ by applying a sudden voltage. As a result, a deformed Leidenfrost vapor layer is generated along the heater. Hence, the surface tension denoted by 13a and 13b works on the upper corner of the protrusion, and the net force denoted by 14 (based on Newton's third law) works on the droplet. Similarly, the net force denoted by 15 works on the droplet at the lower corner. Consequently, a net force of $\sim 2\gamma\phi$ is generated, and the droplet is shot in the left direction with a velocity of $\sim 2\gamma\phi\Delta t/m_p$, where Δt is the time that the droplet is pushed out from the side-shooter. From Fig. 5(d), we can see that $\Delta t \sim \Delta t_w \sim 20\,\mathrm{ms}$, $\gamma \sim 60\,\mathrm{mN/m}$, $\phi \sim 5\,\mathrm{mm}$, and $m_p \sim 6 \times 10^{-5}\,\mathrm{kg}$, and we obtain the velocity as $v_p \sim 2\gamma\phi\Delta t/m_p \sim 0.1\,\mathrm{m/s}$; i.e., we can realize an active side-shooter that shoots the droplet with a velocity of $\sim 0.1\,\mathrm{m/s}$. Namely, the side-shooting phenomenon is applied to both active and passive side-shooters, and the side-shooting phenomenon is generally defined as an acceleration phenomenon caused by the deformed Leidenfrost vapor layer along the nonflat surface, which has a temperature above the Leidenfrost temperature. Note that a simple vertical hot wall cannot relaunch a droplet because the kinetic energy of the droplet is almost lost by the droplet-wall collision. (See the supplementary material for the videos.)

Since the side-shooting phenomenon is an acceleration phenomenon caused by the deformed Leidenfrost vapor layer,

we can use this principle for various actuators in the future. Specifically, by setting several hot oblique protrusions on a water layer in a microfluidic channel, we can accelerate the water as a microfluidic pump. On the other hand, by floating a substrate with several hot protrusions in water, we can move the substrate as a microfluidic container that transports materials. Similarly, we can use this to drive a valve in a microfluidic channel. Here, we mainly consider an active side-shooting phenomenon. However, we can also use a passive-shooting phenomenon to design a new self-propelled motion in the future. For example, by using several hot protrusions that are set on a hot plate in the circumferential direction, we can rotate water as a microfluidic mixer, although we need more extensive studies in the future to realize it. That is, this principle can be applied to a wide range of applications in microfluidics.

VII. CONCLUSION

In conclusion, (1) we observed that a side-shooter with a plate-like hot protrusion launched a water droplet with a high speed ($\sim 15\,\mathrm{cm/s}$). (2) By proposing a simple model that considers the formation of a new surface due to a new Leidenfrost phenomenon coupled with a protrusion, we have successfully explained the side-shooting phenomenon. We believe that our side-shooter is useful in microfluidics.

SUPPLEMENTARY MATERIAL

See the supplementary material for the videos of the side-shooting phenomenon.

ACKNOWLEDGMENTS

REFERENCES

[1]T. Squires and S. Quake, Rev. Mod. Phys. **77**, 977 (2005).
[2]S. Yao, A. M. Myers, J. D. Posner, K. A. Rose, and J. G. Santiago, J. Microelectromech. Syst. **15**, 717 (2006).
[3]J. P. Urbanski, T. Thorsen, J. A. Levian, and M. Z. Bazant, Appl. Phys. Lett. **89**, 143508 (2006).
[4]M. G. Pollack, R. B. Fair, and A. D. Shenderov, Appl. Phys. Lett. **77**, 1725 (2000).
[5]H. Linke, B. J. Alemán, L. D. Melling, M. J. Taormina, M. J. Francis, C. C. Dow-Hygelund, V. Narayanan, R. P. Taylor, and A. Stout, Phys. Rev. Lett. **96**, 154502 (2006).
[6]D. Quéré, Annu. Rev. Fluid Mech. **45**, 197 (2013).
[7]J. T. Ok, E. Lopez-Ona, D. E. Nikitopoulos, H. Wong, and S. Park, Microfluid. Nanofluidics **1**, 1045–1054 (2011).
[8]T. R. Cousins, R. E. Goldstein, J. W. Jaworski, and A. I. Pesci, J. Fluid Mech. **696**, 215–227 (2012).
[9]A. Würger, Phys. Rev. Lett. **107**, 164502 (2011).
[10]S. Hardt, S. Tiwari, and T. Baier, Phys. Rev. E **87**, 063015 (2013).
[11]Q. Li, Q. J. Kang, M. M. Francois, and A. J. Hu, Soft Matter **12**, 302 (2016).
[12]A.-L. Biance, C. Clanet, and D. Quéré, Phys. Fluids **15**, 1632 (2003).
[13]A. Hashmi, Y. Xu, B. Coder, P. A. Osborne, J. Spafford, G. E. Michael, G. Yu, and J. Xu, Sci. Rep. **2**, 797 (2012).

[14]G. G. Wells, R. Ledesma-Aguilar, G. McHale, and K. Sefiane, Nat. Commun. **6**, 639 (2015).

[15]M. Shi, X. Ji, S. Feng, Q. Yang, T. J. Lu, and F. Xu, Sci. Rep. **6**, 28574 (2016).

[16]H. Sugioka and S. Segawa, AIP Adv. **8**, 115209 (2018).

[17]J. M. Arter, D. J. Cleaver, K. Takashina, and A. T. Rhead, Appl. Phys. Lett. **113**, 243704 (2018).

[18]C. Luo, M. Mrinal, and X. Wang, Sci. Rep. **7**, 12018 (2017).

[19]M. Mrinal, X. Wang, and C. Luo, Langmuir **33**, 6307 (2017).

[20]J. T. Pham, M. Paven, S. Wooh, T. Kajiya, H.-J. Butt, and D. Vollmer, Nat. Commun. **8**, 905 (2017).

[21]A. Bouillant, T. Mouterde, P. Bourrianne, A. Lagarde, C. Clanet, and D. Quéré, Nat. Phys. **14**, 1188 (2018).

[22]M. Auliano, M. Fernandino, P. Zhang, and C. A. Dorao, Int. J. Heat Mass Transf. **124**, 307 (2018).

[23]Y. Ge and L.-S. Fan, Phys. Fluids **17**, 027104 (2005).